Available online at www.sciencedirect.com
ScienceDirect
Journal of Colloid and Interface Science 303 (2006) 272–279
JOURNAL OF Colloid and Interface Science
www.elsevier.com/locate/jcis

Numerical simulations of phase separation dynamics in a water–oil–surfactant system

Junseok Kim

Department of Mathematics, Dongguk University, Seoul 100-715, Republic of Korea

Received 10 May 2006; accepted 12 July 2006

Available online 20 July 2006

Abstract

We have studied numerically the dynamics of the microphase separation of a water–oil–surfactant system. We developed an efficient and accurate numerical method for solving the two-dimensional time-dependent Ginzburg–Landau model with two order parameters. The numerical method is based on a conservative, second-order accurate, and implicit finite-difference scheme. The nonlinear discrete equations were solved by using a nonlinear multigrid method. There is, at most, a first-order time step constraint for stability. We demonstrated numerically the convergence of our scheme and presented simulations of phase separation to show the efficiency and accuracy of the new algorithm.

Keywords: Nonlinear multigrid method; Surfactant; Phase separation; Ginzburg–Landau model

1. Introduction

In a water–oil–surfactant system, monolayers of surfactant molecules form microemulsions as a random phase [1]. Microemulsions show two types of morphology as follows. In the symmetric case of even compositions of water and oil, the system shows a cocontinuous network pattern (Fig. 1a). The droplet pattern (Fig. 1b) is found in the asymmetric case of uneven compositions of water and oil.

The dynamics of microphase separation in a water–oil–surfactant system has been investigated numerically by using the time-dependent Ginzburg–Landau (TDGL) model [2]. In [2,3], the cell dynamical system approach is used. A Monte Carlo simulation is used in [4]. In [5], a hybrid model is used, which is a phenomenological semi-microscopic model, where the binary mixture and the surfactant are treated as a continuous field and with discrete molecules, respectively.

In this paper, we present a finite-difference method for the solution of the TDGL model. The Crank–Nicolson method is applied to the temporal discretization. The resulting finite-difference equations are conservative, second-order accurate in space and time, and solved by an efficient and accurate nonlinear multigrid method. An advantage of using a nonlinear multigrid method is that the scheme is much more efficient than traditional iterative solvers in solving the nonlinear equations at the implicit time step. It is straightforward to extend a two-dimensional code to a three-dimensional one and to parallelize the serial code. It is also natural to incorporate hydrodynamic effects such as surface tension force, gravity, and shear flow in this model [6].

The contents of this paper are as follows: in Section 2, we briefly review the governing equations. In Section 3, we consider a fully discrete semi-implicit finite-difference scheme and describe a nonlinear multigrid V-cycle algorithm for the TDGL system. Numerical experiments such as a second-order convergence test and tests of the effects of parameters on the phase separation of the system are performed in Section 4. In Section 5, conclusions are given. In addition, we present a future direction for this current algorithm. The future plan is to incorporate hydrodynamic effects.

2. Governing equations

The dynamics of microphase separation in microemulsion systems can be modeled by the following TDGL model with two order parameters, $\Psi(\mathbf{x}, t)$ and $\Phi(\mathbf{x}, t)$. These parameters

E-mail address: cfdkim@dongguk.edu.
URL: http://math.uci.edu/~jskim/.

0021-9797/$ – see front matter
doi:10.1016/j.jcis.2006.07.032

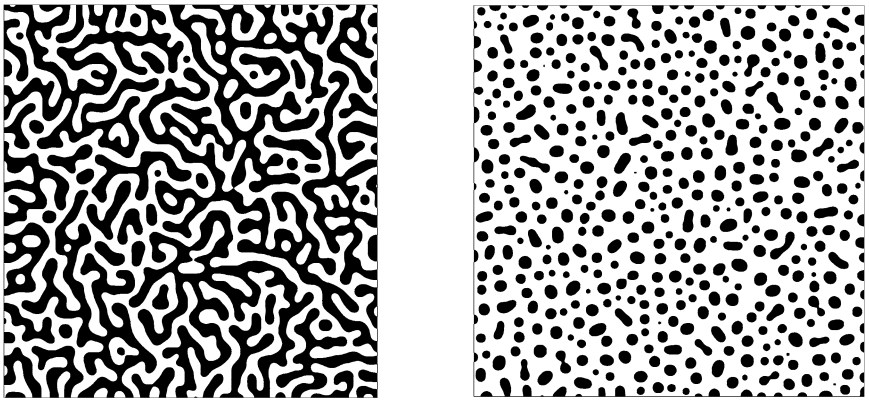

(a) (b)

Fig. 1. Snapshot pictures of the system obtained by the computer simulations for (a) cocontinuous network and (b) droplet/matrix pattern.

describe the difference in the local densities of water and oil and the local concentration of surfactant at site $\mathbf{x}$ and time t, respectively [3]:

$$\mathcal{E}(\Psi,\Phi)=\int_{\Omega}\big[F(\Psi,\Phi)+D_{\Psi}(1-s\Phi)|\nabla\Psi|^2+D_{\Phi}|\nabla\Phi|^2\big]\,\mathrm{d}\mathbf{x}, \tag{1}$$

$$F(\Psi,\Phi)=g\Psi^4-\big[\beta-\nu(\Phi-\Phi_{\mathrm{ave}})\big]\Psi^2+\lambda(\Phi-\Phi_{\mathrm{ave}})^2, \tag{2}$$

where s, g, β, ν, λ, and $D_{\Psi,\Phi}$ are positive phenomenological parameters and Ω is the system domain. In $\mathcal{E}(\Psi,\Phi)$, the term $-sD_{\Psi}\Phi|\nabla\Psi|^2$ energetically prefers a relatively high value of Φ at the interface. In $F(\Psi,\Phi)$, the term $\lambda(\Phi-\Phi_{\mathrm{ave}})^2$ prevents surfactants from forming clusters. The term $\nu(\Phi-\Phi_{\mathrm{ave}})\Psi^2$ means the local coupling interactions. Notations Ψ_{ave} and Φ_{ave} correspond to the Ψ and Φ field values averaged in space, respectively. The TDGL equations in the conserved system are written explicitly as

$$\frac{\partial\Psi}{\partial t}=M_{\Psi}\Delta\frac{\delta\mathcal{E}}{\delta\Psi}, \tag{3}$$

$$\frac{\partial\Phi}{\partial t}=M_{\Phi}\Delta\frac{\delta\mathcal{E}}{\delta\Phi}, \tag{4}$$

$$\frac{\delta\mathcal{E}}{\delta\Psi}=\frac{\partial F(\Psi,\Phi)}{\partial\Psi}-2D_{\Psi}\nabla\cdot\big[(1-s\Phi)\nabla\Psi\big], \tag{5}$$

$$\frac{\delta\mathcal{E}}{\delta\Phi}=\frac{\partial F(\Psi,\Phi)}{\partial\Phi}-2D_{\Phi}\Delta\Phi-D_{\Psi}s|\nabla\Psi|^2, \tag{6}$$

where $M_{\Psi,\Phi}$ are the positive diffusional mobilities. The boundary conditions for the TDGL system are the zero Neumann boundary conditions

$$\mathbf{n}\cdot\nabla\Psi=\mathbf{n}\cdot\nabla\Phi=\mathbf{n}\cdot\nabla\frac{\delta\mathcal{E}}{\delta\Psi}=\mathbf{n}\cdot\nabla\frac{\delta\mathcal{E}}{\delta\Phi}=0\quad\text{on }\partial\Omega\times(0,T), \tag{7}$$

where $\mathbf{n}$ is the normal vector to $\partial\Omega$. Using these boundary conditions, we can derive the following equation [7]:

$$\frac{\mathrm{d}\mathcal{E}(\Psi,\Phi)}{\mathrm{d}t}=-\int_{\Omega}\left(M_{\Psi}\left|\nabla\frac{\delta\mathcal{E}}{\delta\Psi}\right|^2+M_{\Phi}\left|\nabla\frac{\delta\mathcal{E}}{\delta\Phi}\right|^2\right)\mathrm{d}\mathbf{x}, \tag{8}$$

which means the total energy of the system decreases with respect to time.

3. Numerical solution

We first discretize the TDGL system (3)–(6) in space $\Omega=[a,b]\times[c,d]$. Let $[a,b]$ and $[c,d]$ be partitioned by

$$a=x_{1/2}<x_{3/2}<\cdots<x_{N_x+1/2}=b\quad\text{and}$$

$$c=y_{1/2}<y_{3/2}<\cdots<y_{N_y+1/2}=d.$$

For simplicity, we assume the above partitions are uniform in both directions, that is,

$$x_{i+1/2}-x_{i-1/2}=y_{j+1/2}-y_{j-1/2}=h=\frac{b-a}{N_x}$$

$$\text{for } 1\leqslant i\leqslant N_x,\ 1\leqslant j\leqslant N_y.$$

Therefore, $x_{i+1/2}$ and $y_{j+1/2}$ can be represented as $x_{i+1/2}=a+ih$ and $y_{j+1/2}=c+jh$.

We denote by $\Omega_h=\{(x_i,y_j)\colon\ 1\leqslant i\leqslant N_x,\ 1\leqslant j\leqslant N_y\}$ the set of cell centered points $(x_i,y_j)=((x_{i-1/2}+x_{i+1/2})/2,(y_{j-1/2}+y_{j+1/2})/2)$.

For Neumann boundary value problems, it is natural to compute numerical solutions at cell centers. Let Ψ_{ij} be approximations of $\Psi(x_i,y_j)$. We implement the zero Neumann boundary conditions (7) by requiring that, for example,

$$\Psi_{0,j}=\Psi_{1,j},\quad \Psi_{N_x+1,j}=\Psi_{N_x,j},\quad \Psi_{i,0}=\Psi_{i,1},$$

$$\Psi_{i,N_y+1}=\Psi_{i,N_y}\quad\text{for all } i,j.$$

We then define the discrete Laplacian by the standard five-point stencil

$$\Delta_h\Psi_{ij}=(\Psi_{i-1,j}+\Psi_{i+1,j}-4\Psi_{ij}+\Psi_{i,j-1}+\Psi_{i,j+1})/h^2$$

and the discrete l^2-norm by $\|\Psi\|=h\sqrt{\sum_{i=1}^{N_x}\sum_{j=1}^{N_y}\Psi_{ij}^2}$. The TDGL equations (3)–(6) are integrated with respect to time using the Crank–Nicolson method:

$$\frac{\Psi_{ij}^{n+1}-\Psi_{ij}^{n}}{\Delta t}=M_{\Psi}\Delta_h\left(\frac{\delta\mathcal{E}}{\delta\Psi}\right)_{ij}^{n+1/2}, \tag{9}$$

$$\frac{\Phi_{ij}^{n+1}-\Phi_{ij}^{n}}{\Delta t}=M_\Phi\Delta_h\left(\frac{\delta\mathcal{E}}{\delta\Phi}\right)_{ij}^{n+1/2}, \tag{10}$$

$$\begin{aligned}\left(\frac{\delta\mathcal{E}}{\delta\Psi}\right)_{ij}^{n+1/2}&=\frac{\partial F(\Psi_{ij}^{n+1},\Phi_{ij}^{n+1})}{2\partial\Psi}\\&\quad-D_\Psi\nabla_h\cdot\left[\left(1-s\Phi_{ij}^{n+1}\right)\nabla_h^e\Psi_{ij}^{n+1}\right]\\&\quad+\frac{\partial F(\Psi_{ij}^{n},\Phi_{ij}^{n})}{2\partial\Psi}\\&\quad-D_\Psi\nabla_h\cdot\left[\left(1-s\Phi_{ij}^{n}\right)\nabla_h^e\Psi_{ij}^{n}\right],\end{aligned} \tag{11}$$

$$\begin{aligned}\left(\frac{\delta\mathcal{E}}{\delta\Phi}\right)_{ij}^{n+1/2}&=\frac{\partial F(\Psi_{ij}^{n+1},\Phi_{ij}^{n+1})}{2\partial\Phi}+\frac{\partial F(\Psi_{ij}^{n},\Phi_{ij}^{n})}{2\partial\Phi}\\&\quad-D_\Phi\Delta_h\left(\Phi_{ij}^{n+1}+\Phi_{ij}^{n}\right)\\&\quad-\frac{D_\Psi s}{2}\left(\left|\nabla_h^c\Psi_{ij}^{n+1}\right|^2+\left|\nabla_h^c\Psi_{ij}^{n}\right|^2\right),\end{aligned} \tag{12}$$

where ∇_h^e and ∇_h^c are cell-edge and cell-center based discrete gradients, respectively, and are described in Eqs. (16) and (17).

3.1. A nonlinear multigrid V-cycle algorithm

In this section, we develop a nonlinear full approximation storage (FAS) multigrid method to solve the nonlinear discrete system at the implicit time level. The nonlinearity is treated using one step of Newton's iteration and a pointwise Gauss–Seidel relaxation scheme is used as the smoother in the multigrid method. See Ref. [8] for additional details and the following notations.

Let us rewrite Eqs. (9)–(12) as follows:

$$\begin{aligned}&N\left(\Psi^{n+1},\Phi^{n+1},\left(\frac{\delta\mathcal{E}}{\delta\Psi}\right)^{n+1/2},\left(\frac{\delta\mathcal{E}}{\delta\Phi}\right)^{n+1/2}\right)\\&\quad=\left(s_1^n,s_2^n,s_3^n,s_4^n\right),\end{aligned} \tag{13}$$

where the nonlinear system operator (N), the left-hand side of Eq. (13), is defined as

$$\begin{aligned}&\left(\frac{\Psi_{ij}^{n+1}}{\Delta t}-M_\Psi\Delta_h\left(\frac{\delta\mathcal{E}}{\delta\Psi}\right)_{ij}^{n+1/2},\frac{\Phi_{ij}^{n+1}}{\Delta t}-M_\Phi\Delta_h\left(\frac{\delta\mathcal{E}}{\delta\Phi}\right)_{ij}^{n+1/2},\right.\\&\quad\left(\frac{\delta\mathcal{E}}{\delta\Psi}\right)_{ij}^{n+1/2}-\frac{\partial F(\Psi_{ij}^{n+1},\Phi_{ij}^{n+1})}{2\partial\Psi}\\&\qquad+D_\Psi\nabla_h\cdot\left[\left(1-s\Phi_{ij}^{n+1}\right)\nabla_h^e\Psi_{ij}^{n+1}\right],\\&\quad\left(\frac{\delta\mathcal{E}}{\delta\Phi}\right)_{ij}^{n+1/2}-\frac{\partial F(\Psi_{ij}^{n+1},\Phi_{ij}^{n+1})}{2\partial\Phi}\\&\qquad\left.+D_\Phi\Delta_h\Phi_{ij}^{n+1}+\frac{D_\Psi s}{2}\left|\nabla_h^c\Psi_{ij}^{n+1}\right|^2\right),\end{aligned}$$

and the source term, the right-hand side of Eq. (13), is

$$\begin{aligned}&\left(\frac{\Psi_{ij}^{n}}{\Delta t},\frac{\Phi_{ij}^{n}}{\Delta t},\frac{\partial F(\Psi_{ij}^{n},\Phi_{ij}^{n})}{2\partial\Psi}-D_\Psi\nabla_h\cdot\left[\left(1-s\Phi_{ij}^{n}\right)\nabla_h^e\Psi_{ij}^{n}\right],\right.\\&\quad\left.\frac{\partial F(\Psi_{ij}^{n},\Phi_{ij}^{n})}{2\partial\Phi}-D_\Phi\Delta_h\Phi_{ij}^{n}-\frac{D_\Psi s}{2}\left|\nabla_h^c\Psi_{ij}^{n}\right|^2\right).\end{aligned}$$

In the following description of one FAS cycle, we assume that a sequence of grids Ω_k (Ω_{k-1} is coarser than Ω_k by factor 2). Given the number η of pre- and postsmoothing relaxation sweeps, an iteration step for the nonlinear multigrid method using the V-cycle is formally written as follows:

FAS multigrid cycle

$$\begin{aligned}&\left(\Psi_k^{m+1},\Phi_k^{m+1},\left(\frac{\delta\mathcal{E}}{\delta\Psi}\right)_k^{m+1/2},\left(\frac{\delta\mathcal{E}}{\delta\Phi}\right)_k^{m+1/2}\right)\\&\quad=\mathrm{FAScycle}\left(k,\Psi_k^m,\Phi_k^m,\left(\frac{\delta\mathcal{E}}{\delta\Psi}\right)_k^{m-1/2},\left(\frac{\delta\mathcal{E}}{\delta\Phi}\right)_k^{m-1/2},\right.\\&\qquad\left.N_k,s_{1\,k}^n,s_{2\,k}^n,s_{3\,k}^n,s_{4\,k}^n,\eta\right).\end{aligned}$$

That is, $\{\Psi_k^m,\Phi_k^m,(\frac{\delta\mathcal{E}}{\delta\Psi})_k^{m-1/2},(\frac{\delta\mathcal{E}}{\delta\Phi})_k^{m-1/2}\}$ and $\{\Psi_k^{m+1},\Phi_k^{m+1},(\frac{\delta\mathcal{E}}{\delta\Psi})_k^{m+1/2},(\frac{\delta\mathcal{E}}{\delta\Phi})_k^{m+1/2}\}$ are the approximations of $\{\Psi_k^{n+1},\Phi_k^{n+1},(\frac{\delta\mathcal{E}}{\delta\Psi})_k^{n+1/2},(\frac{\delta\mathcal{E}}{\delta\Phi})_k^{n+1/2}\}$ before and after an FAScycle. We now define the FAScycle.

(1) *Presmoothing*

$$\begin{aligned}&\left(\bar\Psi_k^m,\bar\Phi_k^m,\left(\frac{\overline{\delta\mathcal{E}}}{\delta\Psi}\right)_k^{m-1/2},\left(\frac{\overline{\delta\mathcal{E}}}{\delta\Phi}\right)_k^{m-1/2}\right)\\&\quad=\mathrm{SMOOTH}^\eta\left(\Psi_k^m,\Phi_k^m,\left(\frac{\delta\mathcal{E}}{\delta\Psi}\right)_k^{m-1/2},\left(\frac{\delta\mathcal{E}}{\delta\Phi}\right)_k^{m-1/2},\right.\\&\qquad\left.N_k,s_{1\,k}^n,s_{2\,k}^n,s_{3\,k}^n,s_{4\,k}^n\right),\end{aligned}$$

which means performing η smoothing steps with the initial approximations and source terms to get the approximations $\{\bar\Psi_k^m,\bar\Phi_k^m,(\frac{\overline{\delta\mathcal{E}}}{\delta\Psi})_k^{m-1/2},(\frac{\overline{\delta\mathcal{E}}}{\delta\Phi})_k^{m-1/2}\}$. One SMOOTH relaxation operator step consists of solving the system (14)–(17) given below by 4×4 matrix inversion for each ij:

$$\begin{aligned}&\frac{\bar\Psi_{ij}^m}{\Delta t}+\frac{4M_\Psi}{h^2}\left(\frac{\overline{\delta\mathcal{E}}}{\delta\Psi}\right)_{ij}^{m-1/2}\\&\quad=s_{1\,ij}^n+\frac{M_\Psi}{h^2}\left[\left(\frac{\overline{\delta\mathcal{E}}}{\delta\Psi}\right)_{i-1,j}^{m-1/2}+\left(\frac{\delta\mathcal{E}}{\delta\Psi}\right)_{i+1,j}^{m-1/2}\right.\\&\qquad\left.+\left(\frac{\overline{\delta\mathcal{E}}}{\delta\Psi}\right)_{i,j-1}^{m-1/2}+\left(\frac{\delta\mathcal{E}}{\delta\Psi}\right)_{i,j+1}^{m-1/2}\right],\end{aligned} \tag{14}$$

$$\begin{aligned}&\frac{\bar\Phi_{ij}^m}{\Delta t}+\frac{4M_\Phi}{h^2}\left(\frac{\overline{\delta\mathcal{E}}}{\delta\Phi}\right)_{ij}^{m-1/2}\\&\quad=s_{2\,ij}^n+\frac{M_\Phi}{h^2}\left[\left(\frac{\overline{\delta\mathcal{E}}}{\delta\Phi}\right)_{i-1,j}^{m-1/2}+\left(\frac{\delta\mathcal{E}}{\delta\Phi}\right)_{i+1,j}^{m-1/2}\right.\\&\qquad\left.+\left(\frac{\overline{\delta\mathcal{E}}}{\delta\Phi}\right)_{i,j-1}^{m-1/2}+\left(\frac{\delta\mathcal{E}}{\delta\Phi}\right)_{i,j+1}^{m-1/2}\right],\end{aligned} \tag{15}$$

$$
\begin{aligned}
&-\left[\frac{\partial^2 F(\Psi_{ij}^m,\Phi_{ij}^m)}{2\partial\Psi^2}+\frac{D_\Psi}{h^2}\left(4-\frac{s}{2}\big(\bar\Phi_{i-1,j}^m\right.\right.\\
&\qquad\left.\left.+\Phi_{i+1,j}^m+4\Phi_{ij}^m+\bar\Phi_{i,j-1}^m+\Phi_{i,j+1}^m\big)\right)\right]\bar\Psi_{ij}^m\\
&\qquad-\frac{\partial^2 F(\Psi_{ij}^m,\Phi_{ij}^m)}{2\partial\Phi\,\partial\Psi}\bar\Phi_{ij}^m+\left(\overline{\frac{\delta\mathcal{E}}{\delta\Psi}}\right)_{ij}^{m-1/2}\\
&=s_{3\,ij}^n+\frac{\partial F(\Psi_{ij}^m,\Phi_{ij}^m)}{2\partial\Psi}-\frac{\partial^2 F(\Psi_{ij}^m,\Phi_{ij}^m)}{2\partial\Psi^2}\Psi_{ij}^m\\
&\qquad-\frac{\partial^2 F(\Psi_{ij}^m,\Phi_{ij}^m)}{2\partial\Phi\,\partial\Psi}\Phi_{ij}^m\\
&\qquad-\frac{D_\Psi}{h^2}\left[\left(1-s\frac{\Phi_{ij}^m+\Phi_{i+1,j}^m}{2}\right)\Psi_{i+1,j}^m\right.\\
&\qquad+\left(1-s\frac{\bar\Phi_{i-1,j}^m+\Phi_{ij}^m}{2}\right)\bar\Psi_{i-1,j}^m\\
&\qquad+\left(1-s\frac{\Phi_{ij}^m+\Phi_{i,j+1}^m}{2}\right)\Psi_{i,j+1}^m\\
&\qquad\left.+\left(1-s\frac{\bar\Phi_{i,j-1}^m+\Phi_{ij}^m}{2}\right)\bar\Psi_{i,j-1}^m\right],
\end{aligned}
\tag{16}
$$

$$
\begin{aligned}
&-\frac{\partial^2 F(\Psi_{ij}^m,\Phi_{ij}^m)}{2\partial\Psi\,\partial\Phi}\bar\Psi_{ij}^m-\left(\frac{4D_\Phi}{h^2}+\frac{\partial^2 F(\Psi_{ij}^m,\Phi_{ij}^m)}{2\partial\Phi^2}\right)\bar\Phi_{ij}^m\\
&\qquad+\left(\overline{\frac{\delta\mathcal{E}}{\delta\Phi}}\right)_{ij}^{m-1/2}\\
&=s_{4\,ij}^n+\frac{\partial F(\Psi_{ij}^m,\Phi_{ij}^m)}{2\partial\Phi}-\frac{\partial^2 F(\Psi_{ij}^m,\Phi_{ij}^m)}{2\partial\Psi\,\partial\Phi}\Psi_{ij}^m\\
&\qquad-\frac{\partial^2 F(\Psi_{ij}^m,\Phi_{ij}^m)}{2\partial\Phi^2}\Phi_{ij}^m\\
&\qquad-\frac{D_\Phi}{h^2}\big(\Phi_{i+1,j}^m+\bar\Phi_{i-1,j}^m+\Phi_{i,j+1}^m+\bar\Phi_{i,j-1}^m\big)\\
&\qquad-\frac{D_\Psi s}{8h^2}\big(\big(\Psi_{i+1,j}^m-\bar\Psi_{i-1,j}^m\big)^2+\big(\Psi_{i,j+1}^m-\bar\Psi_{i,j-1}^m\big)^2\big).
\end{aligned}
\tag{17}
$$

(2) *Compute the defect*

$$
\begin{aligned}
&\big(\overline{\mathrm{def}}_{1\,k}^m,\overline{\mathrm{def}}_{2\,k}^m,\overline{\mathrm{def}}_{3\,k}^m,\overline{\mathrm{def}}_{4\,k}^m\big)=\big(s_{1\,k}^n,s_{2\,k}^n,s_{3\,k}^n,s_{4\,k}^n\big)\\
&\quad-N_k\left(\bar\Psi_k^m,\bar\Phi_k^m,\left(\overline{\frac{\delta\mathcal{E}}{\delta\Psi}}\right)_k^{m-1/2},\left(\overline{\frac{\delta\mathcal{E}}{\delta\Phi}}\right)_k^{m-1/2}\right).
\end{aligned}
$$

(3) *Restrict the defect and* $\{\bar\Psi_k^m,\bar\Phi_k^m,(\overline{\frac{\delta\mathcal{E}}{\delta\Psi}})_k^{m-1/2},(\overline{\frac{\delta\mathcal{E}}{\delta\Phi}})_k^{m-1/2}\}$

$$
\begin{aligned}
&\big(\overline{\mathrm{def}}_{1\,k-1}^m,\overline{\mathrm{def}}_{2\,k-1}^m,\overline{\mathrm{def}}_{3\,k-1}^m,\overline{\mathrm{def}}_{4\,k-1}^m\big)\\
&\quad=I_k^{k-1}\big(\overline{\mathrm{def}}_{1\,k}^m,\overline{\mathrm{def}}_{2\,k}^m,\overline{\mathrm{def}}_{3\,k}^m,\overline{\mathrm{def}}_{4\,k}^m\big),\\
&\left(\bar\Psi_{k-1}^m,\bar\Phi_{k-1}^m,\left(\overline{\frac{\delta\mathcal{E}}{\delta\Psi}}\right)_{k-1}^{m-1/2},\left(\overline{\frac{\delta\mathcal{E}}{\delta\Phi}}\right)_{k-1}^{m-1/2}\right)\\
&\quad=I_k^{k-1}\left(\bar\Psi_k^m,\bar\Phi_k^m,\left(\overline{\frac{\delta\mathcal{E}}{\delta\Psi}}\right)_k^{m-1/2},\left(\overline{\frac{\delta\mathcal{E}}{\delta\Phi}}\right)_k^{m-1/2}\right).
\end{aligned}
$$

The restriction operator I_k^{k-1} maps k-level functions to the $(k-1)$-level functions.

$$
\begin{aligned}
d_{k-1}(x_i,y_j)&=I_k^{k-1}d_k(x_i,y_j)\\
&=\frac{1}{4}\big[d_k(x_{i-1/2},y_{j-1/2})+d_k(x_{i-1/2},y_{j+1/2})\\
&\quad+d_k(x_{i+1/2},y_{j-1/2})+d_k(x_{i+1/2},y_{j+1/2})\big].
\end{aligned}
$$

Coarse grid values are obtained by averaging the four nearby fine grid values.

(4) *Compute the right-hand side*

$$
\begin{aligned}
&\big(s_{1\,k-1}^n,s_{2\,k-1}^n,s_{3\,k-1}^n,s_{4\,k-1}^n\big)\\
&\quad=\big(\overline{\mathrm{def}}_{1\,k-1}^m,\overline{\mathrm{def}}_{2\,k-1}^m,\overline{\mathrm{def}}_{3\,k-1}^m,\overline{\mathrm{def}}_{4\,k-1}^m\big)\\
&\qquad+N_{k-1}\left(\bar\Psi_{k-1}^m,\bar\Phi_{k-1}^m,\left(\overline{\frac{\delta\mathcal{E}}{\delta\Psi}}\right)_{k-1}^{m-1/2},\left(\overline{\frac{\delta\mathcal{E}}{\delta\Phi}}\right)_{k-1}^{m-1/2}\right).
\end{aligned}
$$

(5) *Compute an approximate solution* $\{\hat\Psi_{k-1}^m,\hat\Phi_{k-1}^m,(\frac{\hat{\delta\mathcal{E}}}{\delta\Psi})_{k-1}^{m-1/2},(\frac{\hat{\delta\mathcal{E}}}{\delta\Phi})_{k-1}^{m-1/2}\}$ *of the coarse grid equation on* Ω_{k-1}, *i.e.*,

$$
\begin{aligned}
&N_{k-1}\left(\Psi_{k-1}^m,\Phi_{k-1}^m,\left(\frac{\delta\mathcal{E}}{\delta\Psi}\right)_{k-1}^{m-1/2},\left(\frac{\delta\mathcal{E}}{\delta\Phi}\right)_{k-1}^{m-1/2}\right)\\
&\quad=\big(s_{1\,k-1}^n,s_{2\,k-1}^n,s_{3\,k-1}^n,s_{4\,k-1}^n\big).
\end{aligned}
\tag{18}
$$

If $k=1$, we explicitly invert a 4×4 matrix to obtain the solution. If $k>1$, we solve Eq. (18) by performing a FAS k-grid cycle using $\{\bar\Psi_{k-1}^m,\bar\Phi_{k-1}^m,(\overline{\frac{\delta\mathcal{E}}{\delta\Psi}})_{k-1}^{m-1/2},(\overline{\frac{\delta\mathcal{E}}{\delta\Phi}})_{k-1}^{m-1/2}\}$ as an initial approximation:

$$
\begin{aligned}
&\left(\hat\Psi_{k-1}^{m+1},\hat\Phi_{k-1}^{m+1},\left(\frac{\hat{\delta\mathcal{E}}}{\delta\Psi}\right)_{k-1}^{m+1/2},\left(\frac{\hat{\delta\mathcal{E}}}{\delta\Phi}\right)_{k-1}^{m+1/2}\right)\\
&\quad=\mathrm{FAScycle}\left(k-1,\bar\Psi_{k-1}^m,\bar\Phi_{k-1}^m,\left(\overline{\frac{\delta\mathcal{E}}{\delta\Psi}}\right)_{k-1}^{m-1/2},\right.\\
&\qquad\left.\left(\overline{\frac{\delta\mathcal{E}}{\delta\Phi}}\right)_{k-1}^{m-1/2},N_{k-1},s_{1\,k-1}^n,s_{2\,k-1}^n,s_{3\,k-1}^n,s_{4\,k-1}^n,\eta\right).
\end{aligned}
$$

(6) *Compute the coarse grid correction (CGC)*

$$
\begin{aligned}
\hat v_{1k-1}^m&=\hat\Psi_{k-1}^m-\bar\Psi_{k-1}^m,\\
\hat v_{3k-1}^{m-1/2}&=\left(\frac{\hat{\delta\mathcal{E}}}{\delta\Psi}\right)_{k-1}^{m-1/2}-\left(\overline{\frac{\delta\mathcal{E}}{\delta\Psi}}\right)_{k-1}^{m-1/2},\\
\hat v_{2k-1}^m&=\hat\Phi_{k-1}^m-\bar\Phi_{k-1}^m,\\
\hat v_{4k-1}^{m-1/2}&=\left(\frac{\hat{\delta\mathcal{E}}}{\delta\Phi}\right)_{k-1}^{m-1/2}-\left(\overline{\frac{\delta\mathcal{E}}{\delta\Phi}}\right)_{k-1}^{m-1/2}.
\end{aligned}
$$

(7) *Interpolate the correction*

$$
\big(\hat v_{1k}^m,\hat v_{2k}^m,\hat v_{3k}^m,\hat v_{4k}^m\big)=I_{k-1}^k\big(\hat v_{1k-1}^{m-1/2},\hat v_{2k-1}^{m-1/2},\hat v_{3k-1}^{m-1/2},\hat v_{4k-1}^{m-1/2}\big).
$$

The interpolation operator I_{k-1}^k maps the $(k-1)$-level functions to the k-level functions. Here, the coarse values are simply transferred to the four nearby fine grid points, i.e., $v_k(x_i,y_j)=I_{k-1}^k v_{k-1}(x_i,y_j)=v_{k-1}(x_{i+1/2},y_{j+1/2})$ for i and

j odd-numbered integers. The values at the other node points are given by

$$v_k(x_{i+1}, y_j) = v_k(x_i, y_{j+1}) = v_k(x_{i+1}, y_{j+1}) = v_{k-1}(x_{i+1/2}, y_{j+1/2}),$$

where i and j are odd-numbered integers.

(8) *Compute the corrected approximation on* Ω_k

$$\Psi_k^{m,\text{ after CGC}} = \bar{\Psi}_k^m + \hat{v}_{1k}^m,$$

$$\left(\frac{\delta\mathcal{E}}{\delta\Psi}\right)_k^{m-1/2,\text{ after CGC}} = \left(\frac{\overline{\delta\mathcal{E}}}{\delta\Psi}\right)_k^{m-1/2} + \hat{v}_{3k}^{m-1/2}.$$

$$\Phi_k^{m,\text{ after CGC}} = \bar{\Phi}_k^m + \hat{v}_{2k}^m,$$

$$\left(\frac{\delta\mathcal{E}}{\delta\Phi}\right)_k^{m-1/2,\text{ after CGC}} = \left(\frac{\overline{\delta\mathcal{E}}}{\delta\Phi}\right)_k^{m-1/2} + \hat{v}_{4k}^{m-1/2}.$$

(9) *Postsmoothing*

$$\left(\Psi_k^{m+1}, \Phi_k^{m+1}, \left(\frac{\delta\mathcal{E}}{\delta\Psi}\right)_k^{m+1/2}, \left(\frac{\delta\mathcal{E}}{\delta\Phi}\right)_k^{m+1/2}\right) = \text{SMOOTH}^{\eta}\left(\Psi_k^{m,\text{ after CGC}}, \Phi_k^{m,\text{ after CGC}}, \left(\frac{\delta\mathcal{E}}{\delta\Psi}\right)_k^{m-1/2,\text{ after CGC}}, \left(\frac{\delta\mathcal{E}}{\delta\Phi}\right)_k^{m-1/2,\text{ after CGC}}, N_k, s_{1k}^n, s_{2k}^n, s_{3k}^n, s_{4k}^n\right).$$

This completes the description of a nonlinear FAS cycle.

4. Numerical experiments

In this section, we describe how we performed a convergence test of the proposed scheme and present several simulations of phase separation. Above all, we investigate the effects of s and λ on the phase separation. We also describe the surfactant dynamics diffusing into a droplet interfacial region from the outside.

4.1. Convergence test of the proposed scheme

To obtain an estimate of the convergence rate, we performed a number of simulations for a sample problem on a set of increasingly finer grids. The initial condition is given by

$$\Psi(x, y) = 0.1\cos(3x) + 0.4\cos(y),$$
$$\Phi(x, y) = 0.1 \tag{19}$$

on a domain $\Omega = [0, 2\pi] \times [0, 2\pi]$. The numerical solutions are computed on the uniform grids, $h = \pi/2^n$ for $n = 4, 5, 6$, and 7. The uniform time steps, $\Delta t = 0.1h$, $g = 1$, $\beta = 2$, $\nu = 0.1$, $\lambda = 0.25$, $s = 0.1$, $D_{\Psi,\Phi} = 0.0225$, and $M_{\Psi,\Phi} = 1$ are used to establish the convergence rates. For each case, the calculations are run to time $T = 0.1$. In our formulation of the method for the TDGL system, since a cell-centered grid is used, we define the error to be the discrete l_2-norm of the difference between that grid and the average of the next finer grid cells covering it:

$$e_{h/\frac{h}{2}ij} \stackrel{\text{def}}{=} \Psi_{hij} - \left(\Psi_{\frac{h}{2}2i,2j} + \Psi_{\frac{h}{2}2i-1,2j} + \Psi_{\frac{h}{2}2i,2j-1} + \Psi_{\frac{h}{2}2i-1,2j-1}\right)/4.$$

The rate of convergence is defined as the ratio of successive errors:

$$\log_2\left(||e_{h/\frac{h}{2}}||/||e_{\frac{h}{2}/\frac{h}{4}}||\right).$$

The errors and rates of convergence are given in Table 1. The results suggest that the scheme is indeed second-order accurate.

Table 1
l_2-Norm of the errors and convergence rates

Case	32–64	Rate	64–128	Rate	128–256
Ψ	1.0759E−1	2.6481	1.7165E−2	2.0792	4.0618E−3
Φ	2.6155E−3	2.1298	5.9762E−4	1.9966	1.4975E−4

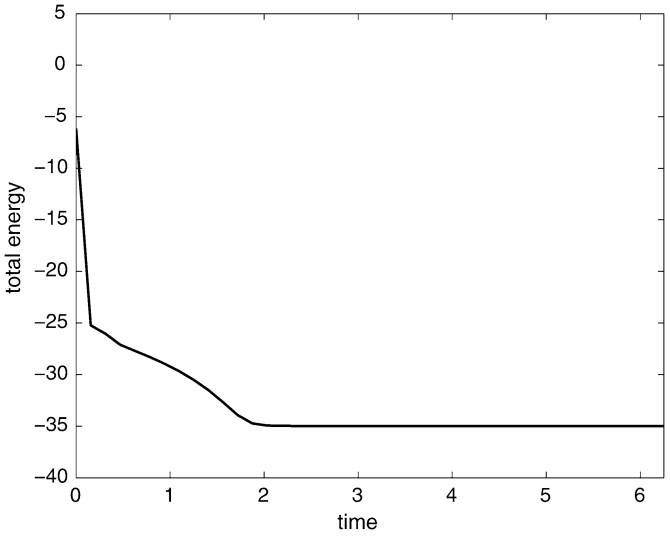

Fig. 2. The time-dependent total energy $\mathcal{E}(\Psi, \Phi)$ of the numerical solutions with the initial data (19).

In Fig. 2, the time evolution of the energy $\mathcal{E}(\Psi, \Phi)$ with same initial data (19) is shown. As expected from Eq. (8), the total energy is nonincreasing and tends to a constant value.

4.2. Spinodal decomposition with off-critical quench

We begin the numerical experiments with an example of spinodal phase separation of a ternary mixture. Here, we consider the effect of λ in the term $\lambda(\Phi - \Phi_{\text{ave}})^2$ in Eq. (2). For the initial condition, we take randomly perturbed concentration fields:

$$\Psi(x, y) = \Psi_{\text{ave}} + 0.01\text{rand}(x, y),$$
$$\Phi(x, y) = \Phi_{\text{ave}} + 0.01\text{rand}(x, y), \tag{20}$$

where the random number function, $\text{rand}(x, y)$, is in $[-1, 1]$ and has zero mean. The $(\Psi_{\text{ave}}, \Phi_{\text{ave}})$ sets are chosen as $(0.2, 0.3)$. The computational domain using a spatial mesh of

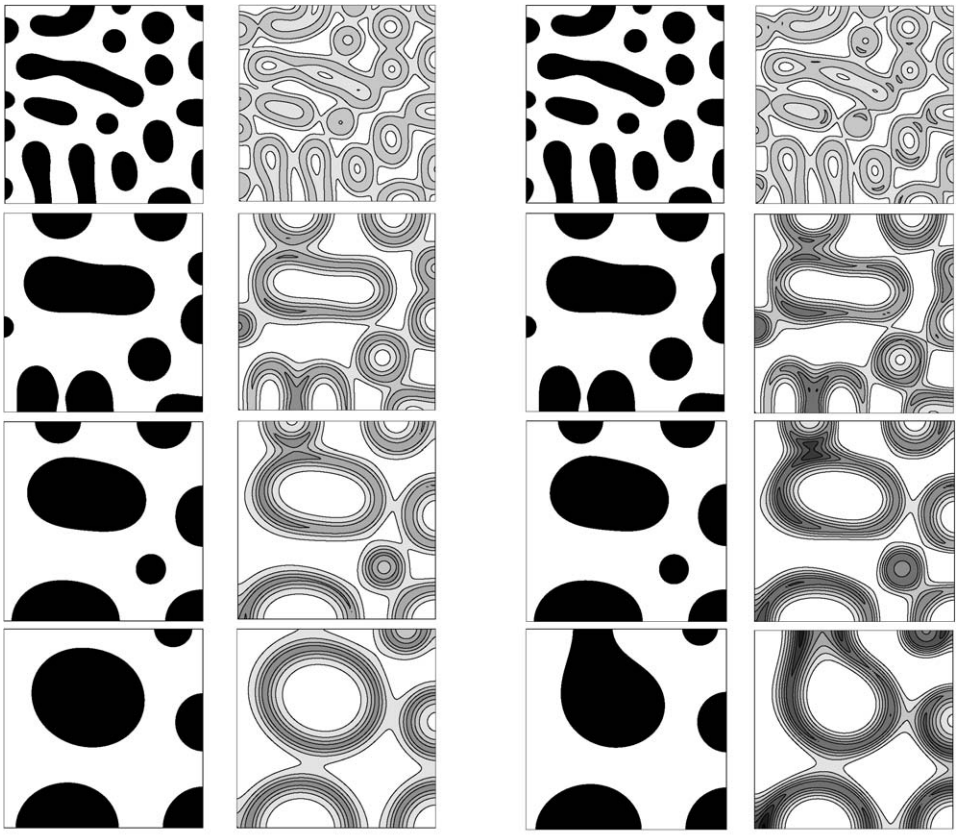

Fig. 3. Columns (a), (b) and columns (c), (d) show the time evolutions of spatial patterns of the Ψ and Φ fields with $\lambda = 0.25$ and $\lambda = 0.05$, respectively. Dark area denotes the region of positive values of Ψ in (a) and higher values of Φ in (b). Times are at $t = 0.4$, 2.0, 3.9, and 7.8.

128×128 is $\Omega = [0, 2\pi] \times [0, 2\pi]$. The uniform time step, $\Delta t = 0.1h$, $g = 1$, $\beta = 2$, $\nu = 0.1$, $s = 0.5$, $D_{\Psi,\Phi} = 0.0225$, and $M_{\Psi,\Phi} = 1$ are used. In Fig. 3, columns (a), (b) and columns (c), (d) show the time evolution of the spatial patterns of the Ψ and Φ fields with $\lambda = 0.25$ and $\lambda = 0.05$, respectively. Dark area denotes the region of positive values of Ψ in (a) and higher values of Φ in (b). The times are at $t = 0.4$, 2.0, 3.9, and 7.8. A moderate value of λ $(= 0.25)$ prevents the surfactants from forming clusters as is shown in Fig. 3b. However, when λ $(= 0.05)$ is too small, the surfactants cluster at some region and change the global dynamics as is shown in Fig. 3d.

Next, we investigate the effect of s in the term $-sD_\Psi \times \Phi|\nabla\Psi|^2$ in Eq. (1). The initial configurations of the Ψ and Φ fields are chosen to be randomly distributed as in Eq. (20) with the $(\Psi_{\text{ave}}, \Phi_{\text{ave}}) = (0.4, 0.3)$ values. All other parameters are the same as before except λ $(= 0.25)$. In Fig. 4, columns (a), (b) and columns (c), (d) show the time evolution of spatial patterns of the Ψ and Φ fields with $s = 0.05$ and $s = 0.5$, respectively. The times are at $t = 0.4$, 1.2, 2.0, and 7.8. The term $-sD_\Psi\Phi|\nabla\Psi|^2$ in Eq. (1) energetically prefers a relatively high value of Φ at the interface. One can see this phenomenon from Figs. 4b and 4d. At the higher value of s $(= 0.5)$, more surfactant accumulates at the interface than in the case of s $(= 0.05)$.

4.3. Quantitative result—domain growth rate

We investigate quantitatively the coarsening manner observed in numerical simulations. The growth of the ordered domains is measured through the average domain size calculated as the inverse of the first moment of the circularly averaged structure factor [5]. Another reliable measure of the characteristic length is the average radius of gyration of the droplets since the droplets are found to be circular in the simulation [2,9]. We use the weighted average radius,

$$R(t) = \frac{\sum_{i=1}^{n} R_i^2}{\sum_{i=1}^{n} R_i}, \quad R_i = \sqrt{\frac{S_i}{\pi}},$$

where S_i is the droplet area and n is the total number of droplets at time t.

The computational domain is $\Omega = [0, 40\pi] \times [0, 40\pi]$ and the mesh size is 256×256 with time step $\Delta t = 0.1h$. All the other parameters are the same as in the previous cases except $(\Psi_{\text{ave}}, \Phi_{\text{ave}}) = (0.4, 0.3)$ and s $(= 0.5)$. To obtain an averaged behavior, ten simulations are run with identical conditions except for the seed of the random number. In Fig. 5, we show the characteristic domain size, $\langle R(t)\rangle$, as a function of time t. The notation $\langle\cdot\rangle$ denotes an average over 10 different initial random conditions. On a log–log plot, the growth appears to be slower than the Lifshitz–Slyozov growth

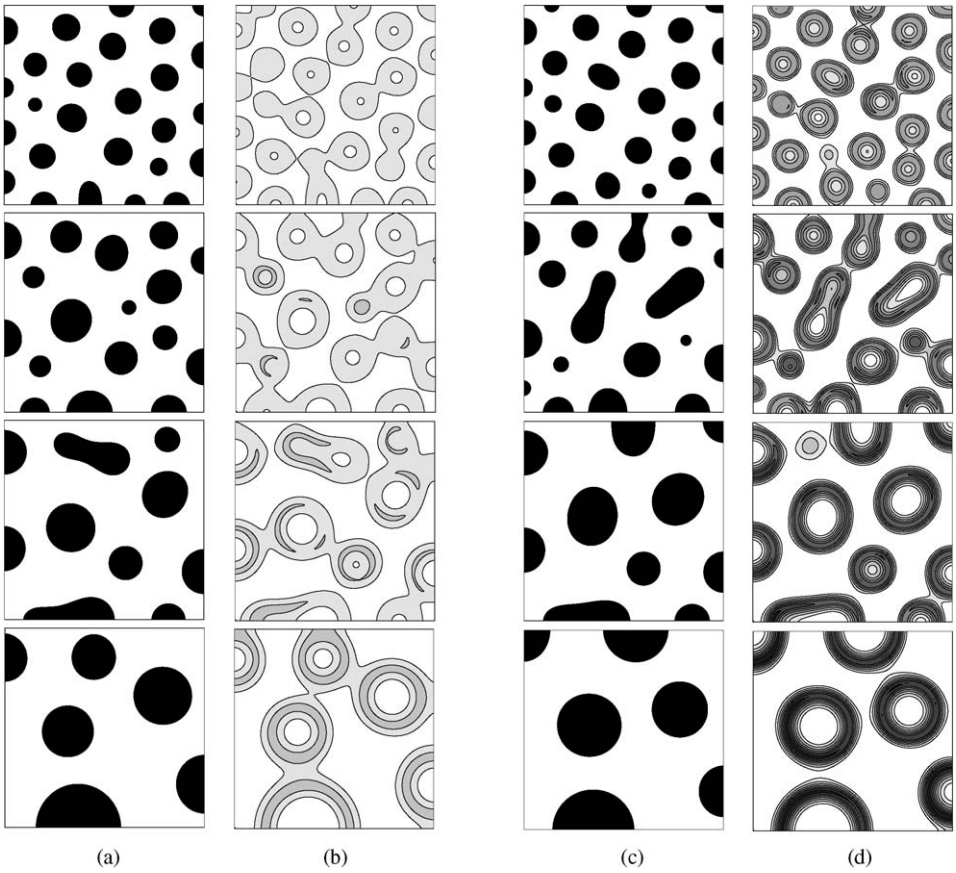

Fig. 4. Columns (a), (b) and columns (c), (d) show the time evolutions of spatial patterns of the Ψ and Φ fields with $s = 0.05$ and $s = 0.5$, respectively. The $(\Psi_{\text{ave}}, \Phi_{\text{ave}})$ sets are chosen as $(0.4, 0.3)$. Times are at $t = 0.4, 1.2, 2.0$, and 7.8.

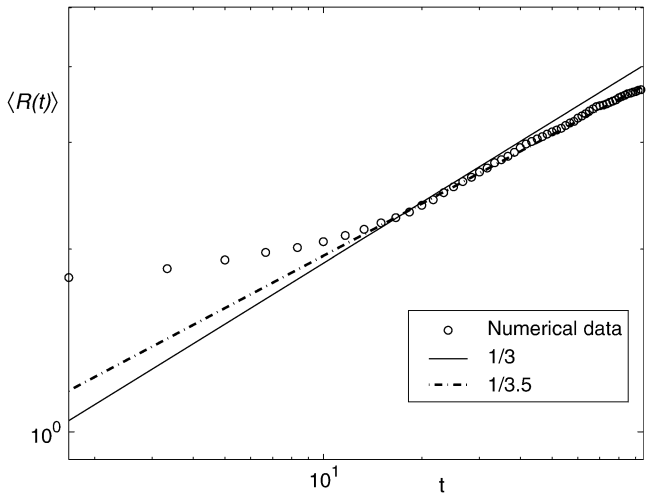

Fig. 5. Time evolution of the mean droplet size $\langle R(t)\rangle$ is shown on a logarithmic-scale plot. The straight line has slope $1/3$ and corresponds to the Lifshitz–Slyozov growth law. The dash–dot line has slope $1/3.5$.

law $\langle R(t)\rangle \sim t^{1/3}$. We observe a slight decrease in the exponent, $\langle R(t)\rangle \sim t^{1/3.5}$. This finding is consistent with previous results [10,11]. For example, previous results using a lattice gas model have shown that the surfactant slows down the growth [11].

4.4. Diffusion of surfactant into the droplet interfacial region

Finally, we discuss the diffusion of the surfactant into the droplet interfacial region. We have an initial condition as follows:

$$\Psi(x, y) = \tanh \frac{1 - \sqrt{(x-\pi)^2 + (y-\pi)^2}}{0.5\sqrt{2D_\Psi}},$$

$$\Phi(x, y) = 0.5\left(1 + \tanh \frac{1 - \sqrt{x^2 + y^2}}{0.5\sqrt{2D_\Phi}}\right).$$

The computational domain using a spatial mesh of 128×128 is $\Omega = [0, 2\pi] \times [0, 2\pi]$. The uniform time step, $\Delta t = 0.3h$, $g = 1$, $\beta = 2$, $\nu = 0.01$, $s = 0.2$, $\lambda = 5$, $D_{\Psi,\Phi} = 0.01$, and $M_{\Psi,\Phi} = 1$ are used. Fig. 6 shows the time evolution of the surfactant diffusion into the droplet interfacial region. The times are at $t = 0.00, 0.12, 0.23, 0.35, 0.47, 0.70, 1.17$, and 4.69 (from left to right and top to bottom order). Initially, there are a droplet in the center of the domain and one quarter of disk of surfactant at the left bottom corner. As the time goes on, the surfactant concentration diffuses to the bulk region and accumulates at the interfacial region of the droplet.

5. Conclusions

We have presented a numerical method for solving the TDGL model. The numerical scheme is finite difference and is

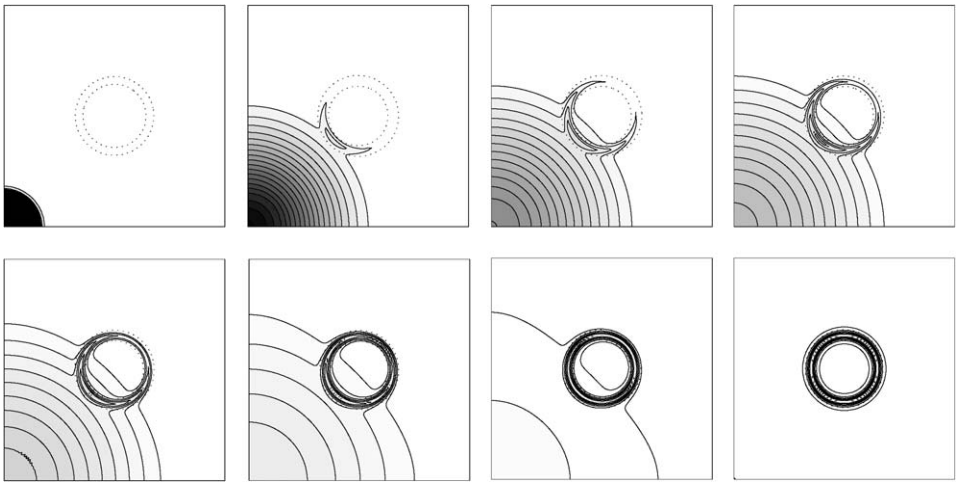

Fig. 6. Surfactant diffusion into the droplet interfacial region. Dotted circles are interfacial region and filled contour lines are surfactant concentration. The higher value of concentration is, the darker color is. The times are at $t = 0.00, 0.12, 0.23, 0.35, 0.47, 0.70, 1.17$, and 4.69 (from left to right and top to bottom order).

solved by an efficient and accurate nonlinear multigrid method. Numerical experiments showed that the scheme is second-order in both space and time and has only a first-order time step restriction. We have studied the effects of parameters, λ and s, on the dynamics of phase separation for a water–oil–surfactant system. A moderate value of λ prevents the surfactants from forming clusters. When λ is too small, the surfactants cluster at some region. This clustering changes the global dynamics. At a higher value of s, more surfactant accumulates at the interface than at a lower value of s. We also described diffusion of surfactant into the stationary droplet interfacial region.

We view the work presented here as preparatory for a study of three component liquids such as two immiscible fluids and one surfactant system with hydrodynamics. In a companion paper [12], we will describe coupling the ternary TDGL model to the equations of fluid flow (Navier–Stokes equations) to simulate the hydrodynamics of flows consisting of three components. Such a system is governed by

$$\nabla \cdot \mathbf{u} = 0,$$

$$\rho(\Psi)(\mathbf{u}_t + \mathbf{u}\cdot\nabla\mathbf{u}) = -\nabla p + \nabla\cdot\left[\eta(\Psi)(\nabla\mathbf{u} + \nabla\mathbf{u}^T)\right] - \alpha D_\Psi \sigma(\Phi)\nabla\cdot\left(\frac{\nabla\Psi}{|\nabla\Psi|}\right)|\nabla\Psi|\nabla\Psi + \rho(\Psi)\mathbf{g},$$

$$\frac{\partial\Psi}{\partial t} + \mathbf{u}\cdot\nabla\Psi = M_\Psi \Delta\frac{\delta\mathcal{E}}{\delta\Psi},$$

$$\frac{\partial\Phi}{\partial t} + \mathbf{u}\cdot\nabla\Phi = M_\Phi \Delta\frac{\delta\mathcal{E}}{\delta\Phi},$$

$$\frac{\delta\mathcal{E}}{\delta\Psi} = \frac{\partial F(\Psi,\Phi)}{\partial\Psi} - 2D_\Psi\nabla\cdot\left[(1-s\Phi)\nabla\Psi\right],$$

$$\frac{\delta\mathcal{E}}{\delta\Phi} = \frac{\partial F(\Psi,\Phi)}{\partial\Phi} - 2D_\Phi\Delta\Phi - D_\Psi s|\nabla\Psi|^2,$$

where $\mathbf{u}$ is the velocity, $\rho(\Psi)$ is the density, $\eta(\Psi)$ is the viscosity, p is the pressure, α is a constant, $\sigma(\Phi)$ is the surface tension coefficient, and $\mathbf{g}$ is the gravity vector. The term $-\alpha D_\Psi\sigma(\Phi)\nabla\cdot(\frac{\nabla\Psi}{|\nabla\Psi|})|\nabla\Psi|\nabla\Psi$ accounts for the interfacial capillary force.

Acknowledgment

This work is supported by the Dongguk University Research Fund.

References

[1] S. Komura, H. Seto, T. Takeda, M. Nagao, Y. Ito, M. Imai, J. Chem. Phys. 105 (1996) 3264.
[2] T. Teramoto, F. Yonezawa, J. Colloid Interface Sci. 235 (2001) 329.
[3] S. Komura, H. Kodama, Phys. Rev. E 55 (1997) 1722.
[4] T. Kawakatsu, K. Kawasaki, J. Colloid Interface Sci. 148 (1992) 23.
[5] T. Kawakatsu, K. Kawasaki, M. Furusaka, H. Okabayashi, T. Kanaya, J. Chem. Phys. 99 (1993) 8200.
[6] J.S. Kim, J.S. Lowengrub, Interfaces Free Bound. 7 (2005) 435.
[7] Q. Du, R.A. Nicolaides, SIAM J. Numer. Anal. 28 (1991) 1310.
[8] U. Trottenberg, C. Oosterlee, A. Schüller, MULTIGRID, Academic Press, 2001.
[9] A. Chakrabarti, R. Toral, J.D. Gunton, Phys. Rev. E 47 (1993) 3025.
[10] A.N. Emerton, P.V. Coveney, B.M. Boghosian, Phys. Rev. E 55 (1997) 708.
[11] F.W.J. Weig, P.V. Coveney, B.M. Boghosian, Phys. Rev. E 56 (1997) 6877.
[12] J.S. Kim, in preparation.